nature nanotechnology

ARTICLES

https://doi.org/10.1038/s41565-020-00845-5

Identification of LiH and nanocrystalline LiF in the solid–electrolyte interphase of lithium metal anodes

Zulipiya Shadike[1], Hongkyung Lee[2,7], Oleg Borodin[3], Xia Cao[2], Xiulin Fan[4], Xuelong Wang[1], Ruoqian Lin[1], Seong-Min Bak[1], Sanjit Ghose[5], Kang Xu[3], Chunsheng Wang[4], Jun Liu[2,6], Jie Xiao[2,6]✉, Xiao-Qing Yang[1]✉ and Enyuan Hu[1]✉

A comprehensive understanding of the solid–electrolyte interphase (SEI) composition is crucial to developing high-energy batteries based on lithium metal anodes. A particularly contentious issue concerns the presence of LiH in the SEI. Here we report on the use of synchrotron-based X-ray diffraction and pair distribution function analysis to identify and differentiate two elusive components, LiH and LiF, in the SEI of lithium metal anodes. LiH is identified as a component of the SEI in high abundance, and the possibility of its misidentification as LiF in the literature is discussed. LiF in the SEI is found to have different structural features from LiF in the bulk phase, including a larger lattice parameter and a smaller grain size (<3 nm). These characteristics favour Li^+ transport and explain why an ionic insulator, like LiF, has been found to be a favoured component for the SEI. Finally, pair distribution function analysis reveals key amorphous components in the SEI.

Metallic lithium is considered to be the ultimate anode material for next-generation batteries because it has a low redox potential (−3.040 V versus the standard hydrogen electrode) and a high theoretical specific capacity (3,860 mAh g^{-1})[1–4]. The challenge faced by lithium metal anodes is their high reactivity with electrolytes, causing low Coulombic efficiencies (CEs), dendrite growth and 'dead lithium' formation during cycling. It is therefore imperative to form a stable SEI[5,6]. In general, the SEI dictates the kinetics of the lithium-ion transport and Li^0 deposition behaviour, which determine the cell performance[7–9]. In recent years, substantial progress has been made towards improving the stability of the lithium metal anode's SEI such as by using highly concentrated electrolytes[10]. However, despite the numerous techniques that have been developed and applied to SEI characterization, such as cryo-electron microscopy[7,11–13], X-ray photoelectron spectroscopy[14,15], nuclear magnetic resonance[16–18] and atomic force microscopy[19,20], the precise composition of the SEI and its morphology, as well as how electrolytes affect its structure and properties, are still not clearly understood. In particular, the presence or absence of LiH has been debated for a long time[7,8]. The possible formation of LiH in the SEI was first proposed in 1999 (ref. [4]), with the first experimental evidence reported in 2018 (ref. [7]) using cryo-scanning transmission electron microscopy (cryo-STEM) mapping. However, the formation of LiH has remained controversial, as evidenced by multiple publications arguing no LiH observations in SEI[8,12], including one that used a quantitative titration method[8]. It is widely accepted that LiF is a critical component for a stable SEI, but how could it play such a critical role if it is an ionic insulator? In this Article, we show new evidence of the presence of LiH in the SEI of lithium metal cells. We use synchrotron-based X-ray diffraction (XRD), pair distribution function (PDF) analysis and density functional theory (DFT) calculations to study the SEI. The origin of possible misidentification between LiH and LiF is clarified and the unique feature of nanocrystalline SEI-LiF (denoted as $LiF_{(SEI)}$) is identified. Amorphous components from solvent or anion decomposition are analysed.

Identification of crystalline components in the SEI

The lithium metal cells were cycled with low (1 M) and high (5 M) concentrations of lithium bis(fluorosulfonyl)imide (LiFSI) salt in propylene carbonate (PC), dimethyl carbonate (DMC) and 1,2-dimethoxyethane (DME) solvents. Results as shown in Supplementary Fig. 1 demonstrate that the cells cycled in DME-based low-concentration electrolyte (LCE) show relatively higher and more stable CEs than the PC- and DMC-based LCEs. High-concentration electrolytes (HCEs) show much improved CEs compared with their low-concentration counterparts, which is consistent with literature reports.

To correlate the electrochemical performance with SEI formation, it is critical to identify and quantify the SEI components. There are important questions to be answered. Is LiH an important component of the SEI? Are the crystalline form and grain size of LiF in the SEI different from the bulk LiF, and if so, how are they affected by the salt concentration and the type of solvent in the electrolyte? Can we quantify the percentage of metallic lithium, LiF and LiH in the SEI and correlate it with the salt concentration in the electrolyte?

However, the identification and quantification of the SEI face challenges due to there being extremely small sample amounts and

[1]Chemistry Division, Brookhaven National Laboratory, Upton, NY, USA. [2]Energy and Environment Directorate, Pacific Northwest National Laboratory, Richland, WA, USA. [3]Battery Science Branch, Energy and Biomaterials Division, Sensor and Electron Devices Directorate, US Army Research Laboratory, Adelphi, MD, USA. [4]Department of Chemical and Biomolecular Engineering, University of Maryland, College Park, MD, USA. [5]National Synchrotron Light Source II, Brookhaven National Laboratory, Upton, NY, USA. [6]Department of Materials Science and Engineering, University of Washington, Seattle, WA, USA. [7]Present address: Department of Energy Science and Engineering, Daegu Gyeongbuk Institute of Science and Technology (DGIST), Daegu, Republic of Korea. ✉e-mail: jie.xiao@pnnl.gov; xyang@bnl.gov; enhu@bnl.gov

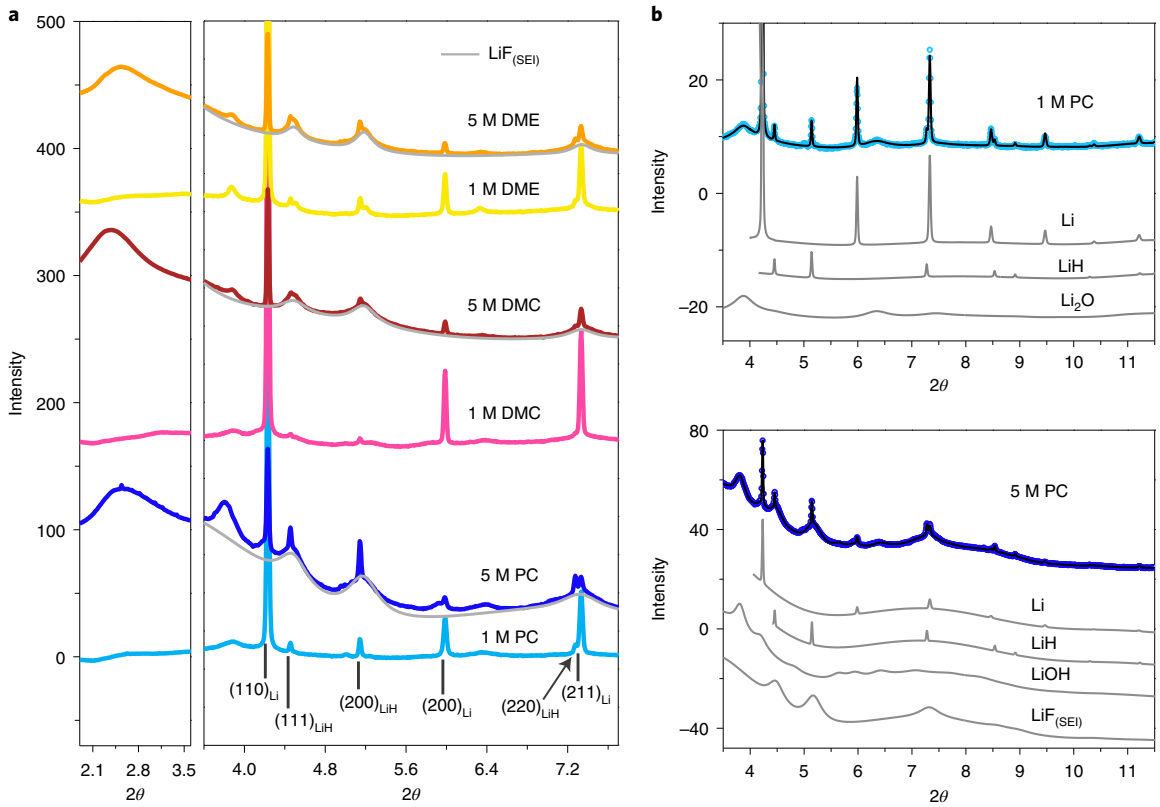

Fig. 1 | Characterization of the interphase by XRD. a, SEI XRD of LCEs and HCEs using LiFSI as the salt and PC, DMC and DME as the solvents. The light grey pattern belongs to $LiF_{(SEI)}$. The wavelength used is 0.18323 Å. **b**, Rietveld refinement of SEI XRD data of low- (upper) and high-concentration (lower) LiFSI in PC. Contributions of individual phases to the XRD pattern are also shown. Open circles, experimental data; black lines, calculated data.

possible radiation damage. An X-ray source of high energy and intensity from a third-generation synchrotron facility can collect high-quality data for a trace amount of sample with little radiation damage[21], as well as providing high-quality PDF data for the analysis of both crystalline and amorphous phases. These X-ray techniques can provide statistical information, which is equally important to the spatial information provided by cryo-transmission electron microscopy (cryo-TEM). XRD patterns of the SEI samples collected from the cells using LCEs and HCEs are shown in Fig. 1a. The XRD patterns of all LCE SEI samples are dominated by sharp Bragg peaks with flat baselines, indicating the dominance of crystalline phases. Since the scattering from the air and the capillary has been deducted as the background, all signals in Fig. 1a come from SEI components. Rietveld refinement of the PC-LCE SEI (Fig. 1b, upper part, and Supplementary Table 1) reveals the coexistence of three crystalline phases: lithium metal, Li_2O and LiH. The low CEs for the PC-LCE sample shown in Supplementary Fig. 1a imply the formation of inactive (or 'dead') Li^0. Li_2O has been identified in the SEI by other techniques and is considered to be decomposition product of the salt and solvent[9]. The most interesting component here is LiH, which shows that the face-centred-cubic (FCC) phase has a lattice parameter of 4.084 Å, matching the value of LiH in the literature[22–24].

For all three HCE SEI samples in Fig. 1a, the striking difference from their LCE counterparts is the appearance of additional broad bumps, which should arise from either amorphous phases or nanocrystallites. The low-angle (<3.5°) bump is attributed to the amorphous phases using PDF analysis (see below). Most of the high-angle (>3.5°) bumps can be modelled well with the LiF crystal structure. Notably, the refined results indicate that this phase is quite different from the bulk LiF and is expressed as SEI-LiF, or $LiF_{(SEI)}$. The $LiF_{(SEI)}$ phase (Fig. 1b, lower part, and Supplementary Fig. 2) has a typical grain size of ~3 nm and a lattice parameter of ~4.05 Å, which is larger than that of bulk LiF (4.026 Å)[25–27]. This larger lattice parameter might be caused by two factors. First, the smaller crystallite size usually results in a larger lattice parameter, as in the case of MgO, Fe_2O_3, CeO_2 and TiO_2[28–30], caused by the interaction between the crystal surface and surrounding chemical species. It has been reported that LiF can be bonded with other chemical species in the SEI region. For example, C=C in ethylene gas produced by the decomposition of ethylene carbonate is able to bond the fluorine atom in LiF, as confirmed by electron energy loss spectroscopy and large bubble formation in the fluorine-rich area[7,31]. Such bonding is likely to influence the lattice parameter. Second, a solid-solution phase of LiH_xF_{1-x} may be formed since both LiH and LiF have the same FCC structure and similar lattice parameters (LiH: 4.084 Å; LiF: 4.026 Å)[24,25]. It has been reported that as much as 0.6 LiH can be dissolved in LiF to form $LiH_{0.6}F_{0.4}$ (ref. [32]). If such a solid solution of LiH and LiF did form, it would substantially increase the ionic conductivity because the Li–H bond is much weaker than the Li–F bond[33].

Confirmation of LiH in the SEI

The existence of LiH in the SEI was further confirmed based on the moisture sensitivity of LiH versus the moisture stability of LiF, using in situ XRD experiments. Figure 2a presents the results of SEI chemical composition evolution upon exposure to moisture. In a glove box, a capillary containing the SEI from a cell using 1 M LiFSI in PC was sealed using epoxy glue before taking it to the synchrotron beamline. The seal of the capillary was opened to air, with a relative humidity of 40%, immediately before data collection. It can be clearly seen that the intensities of the Li^0 peaks decrease with exposure time

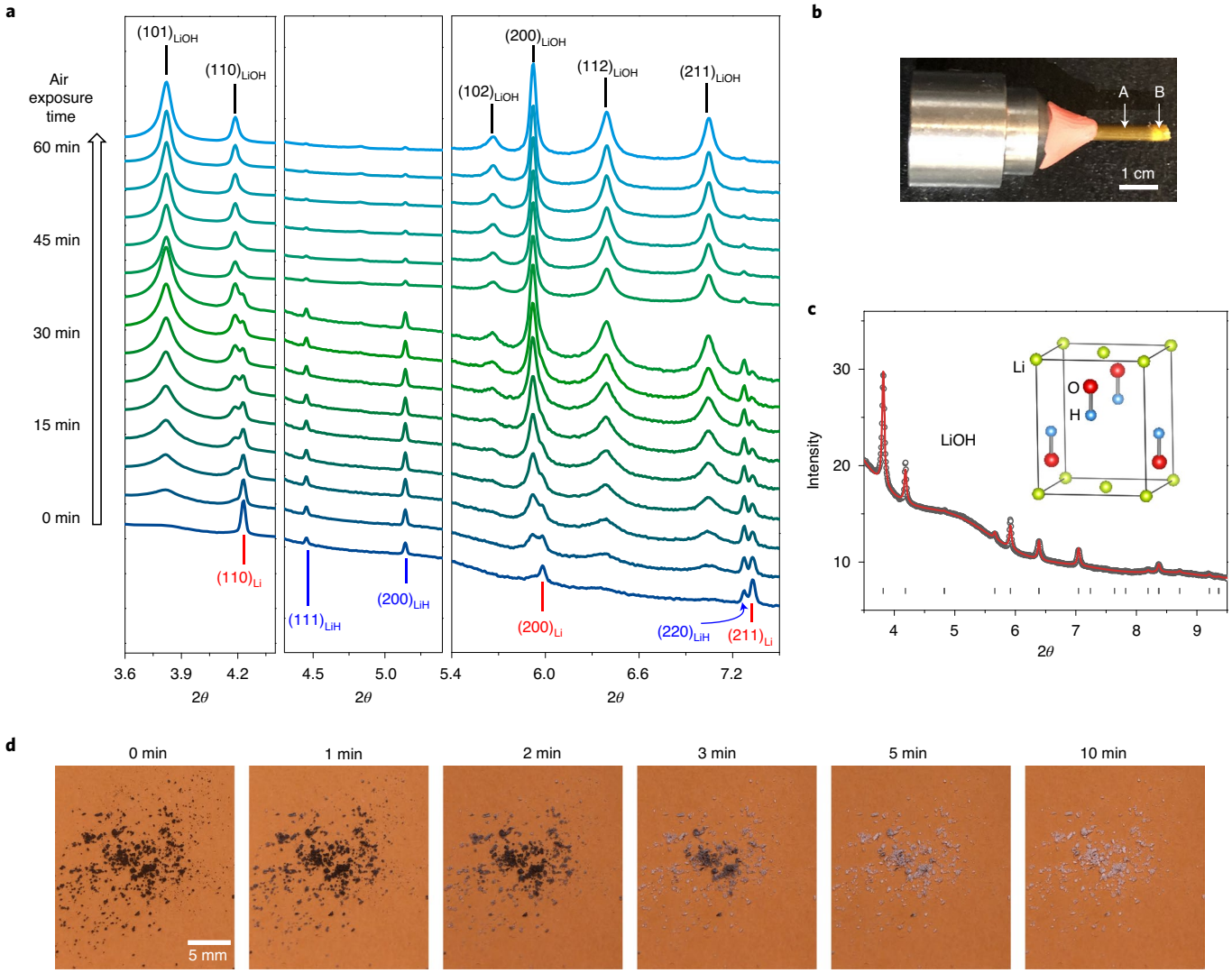

Fig. 2 | Air-exposure experiment of the interphase sample. a, In situ XRD of the SEI sample of 1 M LiFSI in PC. The wavelength used was 0.18323 Å. **b**, Picture of the SEI sample contained in the capillary after exposure for 60 min, where the in situ XRD data were taken from point 'A'. Point 'B' illustrates that the end portion, having direct contact with air, has turned from its initial dark colour to white. **c**, Rietveld refinement of the XRD pattern taken from point 'B' in **b** after exposure for 60 min. The wavelength used was 0.18323 Å. **d**, Colour change of the dispersed SEI sample when it is exposed to air. The orange background is paper.

and totally disappear after 34–38 min of exposure (corresponding to the 10th XRD pattern counting from the bottom), while the intensities of a newly emerging set of peaks representing the LiOH phase increase at the same time. Moreover, after 34–38 min, the intensities of the LiH peaks decrease considerably, and mostly disappear after 60 min. These results provide solid experimental evidence to confirm our identification of LiH in the SEI, because only LiH, and not LiF, can react with moisture to form LiOH. The moisture stability of the $LiF_{(SEI)}$ phase was confirmed by an air-exposure experiment on the HCE SEI for DMC (Supplementary Fig. 3 and Supplementary Table 2). The results of the Rietveld refinement on the HCE SEI after air exposure give us confidence in our fitting model and results in Fig. 1. In Fig. 2a, lithium peaks fading faster than the LiH peaks suggests that Li^0 could be more reactive with moisture than LiH (ref. [7]). Both reactions ended up with the same final product of LiOH. In Fig. 2b area 'A', the SEI sample has its original dark colour. By contrast, area 'B' near the open end of the capillary tube shows that the colour has changed to white, indicating the presence of LiOH. Figure 2c shows an XRD pattern collected at spot 'B' in Fig. 2b, and has an excellent fit with the LiOH structure (Supplementary Table 3). To visualize the air sensitivity of the SEI, originally sealed SEI samples were spread on paper and exposed to air and photos were taken every minute for ten minutes. These photos, in Fig. 2d, show that colour change began within one minute of exposure. After five minutes, almost all the SEI sample had turned from black to white, demonstrating the high air-exposure sensitivity of the SEI and the importance of avoiding exposure to the air. If the SEI samples had been exposed to air for even one minute, they would have decomposed and misidentification would have been inevitable.

Identification of amorphous components in the SEI

Amorphous SEI components were examined using PDF analysis, which can probe atomic pairs regardless of whether they are in a crystalline or amorphous state. PDF results for LCE and HCE SEI samples are shown in Fig. 3. In both cases, the long-range section (10–30 Å, corresponding to crystalline phases with long-range order) can be modelled well based on the phases identified by XRD (Supplementary Fig. 4). The short-range section (1–4 Å) provides

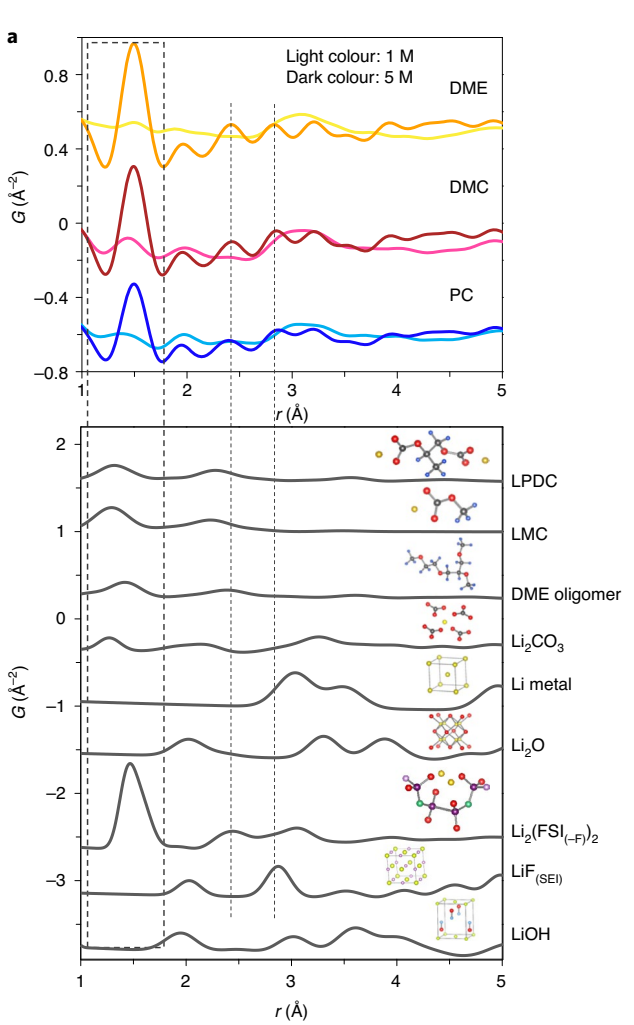

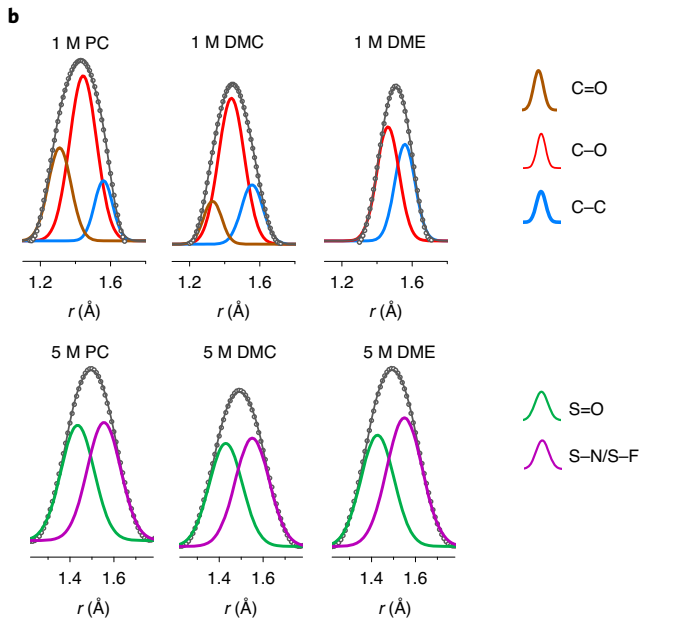

c

Bonds	Related species	Bond length (Å)
C=O double bond	Li_2CO_3, alkyl carbonate	1.28
C–O single bond in the CO_3 moiety	Li_2CO_3, alkyl carbonate	1.36
C–O single bond in the C–O–C moiety	Alkyl carbonate, ether	1.44
C–C single bond	Alkyl carbonate, ether	1.55
S=O double bond	FSI anion	1.43
S–F bond	FSI anion	1.54
S–N bond	FSI anion	1.56

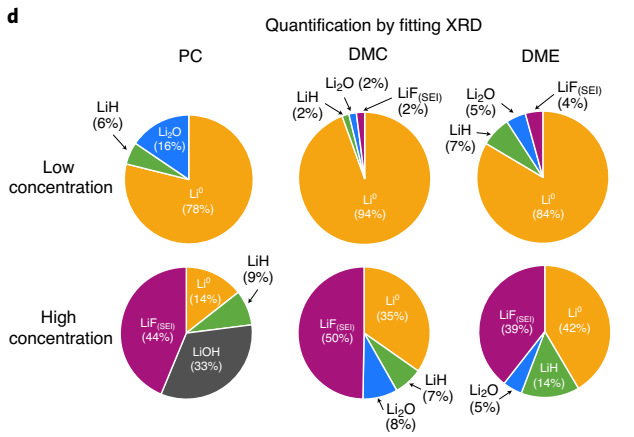

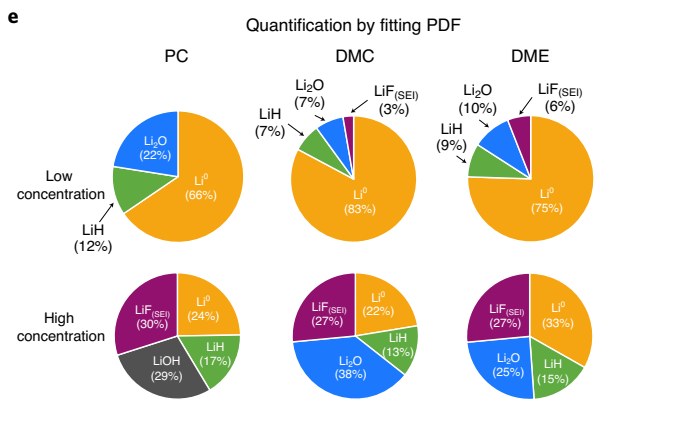

Fig. 3 | Analysis of amorphous components and relative quantification of crystalline components in the interphase. a, Short-range region (amorphous part) of the PDF data (upper part) and calculated PDF data of possible components in the SEI (lower part). The structure of each component is also shown. LPDC, lithium propylene dicarbonate; LMC, lithium methyl carbonate. Atom colour code for all structures: gold, Li; black, C; red, O; blue, H; green, N; light purple, F; dark purple, S. The dominant peaks in the HCE SEI are marked with the dashed-line rectangle and dashed lines. **b**, Fitting of the first PDF peak. Upper and lower parts correspond to LCE and HCE SEIs, respectively. **c**, Possible bonds related to the first PDF peak and their detailed information. **d**, Quantification of the phase fractions (mass fraction) obtained by Rietveld refinement of the XRD data. **e**, Quantification of the phase fractions (mass fraction) by fitting the long-range PDF data (10–30 Å).

information about the amorphous phases with short-range structures only. The LCE SEI and HCE SEI have quite different amorphous components, as indicated by their distinct PDF patterns in the short-range section (upper part of Fig. 3a). PDF pattern of the HCE SEI has a very strong dominant peak at 1.5 Å. By contrast, the PDF peak at this position for the LCE SEI is weaker than the other

peaks. This dominant peak indicates that the atomic pairs corresponding to the 1.5 Å peak must involve atoms with a high atomic number, which is likely to be sulfur. This is further confirmed by comparing experimental data with the calculated PDF pattern of a typical FSI anion-decomposition product, $Li_2(FSI_{(-F)})_2$, where '−F' indicates that one fluorine atom is removed, in which the 1.5 Å peak is the dominant peak and is contributed by sulfur-related atomic pairs like S=O, S–F and S–N. For the HCE SEI, the 1.5 Å peak is the dominant one regardless of the solvent used, suggesting that it is the anion, and not the solvent, that plays the major role in forming the SEI. This point is also supported by analysing the first PDF peak of the HCE SEI (lower part of Fig. 3b). Deconvolution of the peak indicates that the first peak is contributed by the S=O double bond (1.43 Å), and with the second from S–F and S–N bonds (~1.55 Å), all of which originate from reduction of the FSI anion. The 1.36 Å peak, which is present in the PDF of the LCE SEI as a characteristic peak of the carbonyl group, is absent from the HCE SEI and suggests a negligible contribution of the solvent in forming the SEI at high salt concentration. Another piece of evidence for anion decomposition in the HCE SEI is the two peaks at 2.4 and 2.8 Å. Comparing with calculated PDF values of model compounds whose molecular/crystal structures are obtained from DFT calculations, the 2.4 and the 2.8 Å peaks are mainly contributed by the sulfonyl O–O pair in the FSI anion and the F–F pair in $LiF_{(SEI)}$, respectively. Since the sulfonyl group and the fluorine atom can only come from anions, these two peaks provide additional evidence of the critical role of anions in forming the HCE SEI.

The first PDF peak usually has little atomic pair overlap and can be analysed in detail. This first peak is fitted by several possible Gaussian components. As shown in the upper part of Fig. 3b, for carbonates (PC and DMC), the first peak has a lot of contribution from the very low *r* peak centred around 1.36 Å. However, in the case of DME, only two features centred at 1.46 and 1.55 Å contribute exclusively to the first peak. Detailed analysis of the bond lengths relevant to the decomposition species (Fig. 3b,c) reveal that the 1.36 Å peak arises from the C=O double bond in the carbonyl group that is present in both Li_2CO_3 (not found in XRD) and alkyl carbonates. On the other hand, the 1.44 and the 1.55 Å peaks are associated with the C–O single bond in ether and the C–C bond, respectively. These results suggest that both Li_2CO_3 and alkyl carbonates are absent in the SEI formed in the DME-based electrolyte. This is reasonable since both carbonate solvents (PC and DMC) contain the C=O source whereas DME does not.

The quantification of (nano)crystalline components in the SEI is done by fitting the XRD (see Fig. 1b, Supplementary Fig. 2 and Supplementary Tables 1 and 4–8) and long-range PDF data (Supplementary Fig. 4 and Supplementary Tables 9–14) and the results are shown in Fig. 3d and 3e, respectively. For the LCE in PC, the SEI consists mainly of dead Li^0, LiH and Li_2O. However, for DMC and DME, the small amounts of $LiF_{(SEI)}$ in SEI are due to the much weaker interaction between the lithium cation and the solvent that allows the fluorine-containing anion to appear in the vicinity of the lithium-ion solvation, providing a fluorine source to participate in the SEI formation. For the HCE SEI, the $LiF_{(SEI)}$ phase is in high abundance, regardless of the solvent type, showing the clear correlation between the high salt concentration and the high relative $LiF_{(SEI)}$ content, which is also consistent with the high CE value as shown in Supplementary Fig. 1d–f. It is very interesting to note that the relative contents of dead Li^0 for all three HCE SEIs are remarkably reduced compared to those of the LCE SEIs, showing the lithium dendrite (dead Li) suppression effect of the HCE. This is particularly true for the SEI grown in PC at a high salt concentration. Large amounts of LiOH were also observed in the HCE SEI formed in PC, which differs from HCEs in DMC and DME, where Li_2O was found, but not LiOH. This suggests that while anion decomposition and $LiF_{(SEI)}$ formation are more pronounced at high salt concentrations for all three types of solvent, the final decomposition products are dependent on the solvent type. It should be noted that even though both XRD and long-range PDF data can be fitted quite well using the same combination of crystalline phases and the relative contents obtained from both methods show a similar general trend when comparing the LCE and HCE SEIs, the detailed relative contents do have obvious differences, as shown in Fig. 3d,e. This might be caused by the contribution from amorphous phases to the broad peaks assigned to $LiF_{(SEI)}$ in the XRD, resulting in an inflated $LiF_{(SEI)}$ percentage. In PDF analysis, the contributions of amorphous phases are limited in the low '*r*' region. Therefore, when only long-range PDF data were used in the fitting, the calculated phase percentage of nanocrystalline $LiF_{(SEI)}$ was reduced and other components (such as LiH, Li_2O and LiOH) are increased accordingly. Since the amorphous phases (short-range) and crystalline phases (long-range) can be separated in PDF analysis, the relative contents calculated from PDF fitting should be more reliable, especially when nanocrystal phases are involved. However, it is worth noting that, compared with PDF fitting, XRD Rietveld refinement can provide much more accurate lattice parameter values (as suggested by the summary of fitting/refinement results in Supplementary Tables 1 and 4–14), which is critically important in differentiating LiH from $LiF_{(SEI)}$ since they have very close lattice parameter values.

Conclusions

Using XRD and PDF techniques, we have systematically studied the crystalline and amorphous components of SEIs grown in carbonate and ether electrolytes at both low and high salt concentrations. The XRD results clearly identified the existence of crystalline LiH as an important component of the SEI grown in both low and high salt concentrations, and its chemical identity is further confirmed through XRD pattern changes during exposure to moisture. Our X-ray results here not only confirm the existence of LiH in the SEI as identified by previous cryo-TEM work (with spatial resolution)[7], but also establish guidelines for avoiding the misidentification of LiH as LiF in the SEI. The possible reasons for LiH not being identified in previous literature reports may be twofold: first, LiH and LiF have the FCC structure and have a similar lattice parameter (4.084 Å for LiH and 4.026 Å for LiF) and general XRD pattern appearance (Supplementary note and Supplementary Fig. 5); second, LiH is extremely sensitive to ambient air, particularly moisture. Exposure for a very short time (~1 s) could cause the decomposition of LiH, making it undetectable, especially when using surface-sensitive techniques. It should be noted that X-ray techniques generally lack spatial resolution. What this work provides is a statistically reliable chemical picture of the SEI, which complements an earlier report of LiH in the SEI obtained using cryo-TEM techniques[7]. Moreover, a unique XRD pattern with a broader peak shape and a larger lattice parameter than in bulk LiF is identified as a signature of $LiF_{(SEI)}$, which is distinctly different from bulk LiF. Such a feature of $LiF_{(SEI)}$ is attributed to the nanocrystal size and the possible formation of the LiH_xF_{1-x} solid solution in the SEI. Relative quantification shows that the HCE SEI has a higher $LiF_{(SEI)}$ content and less dead lithium than the LCE SEI, resulting in a higher CE and a better electrochemical performance. PDF analysis has demonstrated that the SEI chemistry in the HCE is dominated by the salt-anion-reduction process, which is quite different from the solvent-reduction-dominated process when in the LCE.

Online content

Any methods, additional references, Nature Research reporting summaries, source data, extended data, supplementary information, acknowledgements, peer review information; details of author contributions and competing interests; and statements of data and code availability are available at https://doi.org/10.1038/s41565-020-00845-5.

Received: 3 July 2020; Accepted: 22 December 2020;
Published online: 28 January 2021

References

1. Whittingham, M. S. Ultimate limits to intercalation reactions for lithium batteries. *Chem. Rev.* **114**, 11414–11443 (2014).
2. Liu, J. et al. Pathways for practical high-energy long-cycling lithium metal batteries. *Nat. Energy* **4**, 180–186 (2019).
3. Lin, D., Liu, Y. & Cui, Y. Reviving the lithium metal anode for high-energy batteries. *Nat. Nanotechnol.* **12**, 194–206 (2017).
4. Aurbach, D. & Weissman, I. On the possibility of LiH formation on Li surfaces in wet electrolyte solutions. *Electrochem. Commun.* **1**, 324–331 (1999).
5. Xiao, J. How lithium dendrites form in liquid batteries. *Science* **366**, 426–427 (2019).
6. Liu, B., Zhang, J.-G. & Xu, W. Advancing lithium metal batteries. *Joule* **2**, 833–845 (2018).
7. Zachman, M. J., Tu, Z., Choudhury, S., Archer, L. A. & Kourkoutis, L. F. Cryo-STEM mapping of solid–liquid interfaces and dendrites in lithium-metal batteries. *Nature* **560**, 345–349 (2018).
8. Fang, C. et al. Quantifying inactive lithium in lithium metal batteries. *Nature* **572**, 511–515 (2019).
9. Cheng, X.-B. et al. A review of solid electrolyte interphases on lithium metal anode. *Adv. Sci.* **3**, 1500213 (2016).
10. Borodin, O. et al. Uncharted waters: super-concentrated electrolytes. *Joule* **4**, 69–100 (2020).
11. Wang, X. et al. New insights on the structure of electrochemically deposited lithium metal and its solid electrolyte interphases via cryogenic TEM. *Nano Lett.* **17**, 7606–7612 (2017).
12. Li, Y. et al. Atomic structure of sensitive battery materials and interfaces revealed by cryo-electron microscopy. *Science* **358**, 506–510 (2017).
13. Wang, X. et al. Cryogenic electron microscopy for characterizing and diagnosing batteries. *Joule* **2**, 2225–2234 (2018).
14. Wood, K. N. et al. Operando X-ray photoelectron spectroscopy of solid electrolyte interphase formation and evolution in Li_2S-P_2S_5 solid-state electrolytes. *Nat. Commun.* **9**, 2490 (2018).
15. Nandasiri, M. I. et al. In situ chemical imaging of solid-electrolyte interphase layer evolution in Li–S batteries. *Chem. Mater.* **29**, 4728–4737 (2017).
16. Wan, C. et al. Multinuclear NMR study of the solid electrolyte interface formed in lithium metal batteries. *ACS Appl. Mater. Interfaces* **9**, 14741–14748 (2017).
17. Wang, L. et al. Identifying the components of the solid–electrolyte interphase in Li-ion batteries. *Nat. Chem.* **11**, 789–796 (2019).
18. Ota, H., Sakata, Y., Wang, X., Sasahara, J. & Yasukawa, E. Characterization of lithium electrode in lithium imides/ethylene carbonate and cyclic ether electrolytes: II. surface chemistry. *J. Electrochem. Soc.* **151**, A437–A446 (2004).
19. Shen, C. et al. Direct observation of the growth of lithium dendrites on graphite anodes by operando EC-AFM. *Small Methods* **2**, 1700298 (2018).
20. Liu, T. et al. In situ quantification of interphasial chemistry in Li-ion battery. *Nat. Nanotechnol.* **14**, 50–56 (2019).
21. Sun, Y. & Ren, Y. In situ synchrotron X-ray techniques for real-time probing of colloidal nanoparticle synthesis. *Part. Part. Syst. Charact.* **30**, 399–419 (2013).
22. David, W. I. F. et al. A mechanism for non-stoichiometry in the lithium amide/lithium imide hydrogen storage reaction. *J. Am. Chem. Soc.* **129**, 1594–1601 (2007).
23. Zimmerman, W. B. Lattice-constant dependence on isotopic composition in the ^{7}Li (H, D) system. *Phys. Rev. B* **5**, 4704–4707 (1972).
24. Tyutyunnik, O. I. et al. Lithium hydride single crystal growth by bridgman-stockbarger method using ultrasound. *J. Cryst. Growth* **68**, 741–746 (1984).
25. Srivastava, K.-K. & Merchant, H. D. Thermal expansion of alkali halides above 300°K. *J. Phys. Chem. Solids* **34**, 2069–2073 (1973).
26. Ben Yahia, H. et al. Synthesis and characterization of the crystal structure, the magnetic and the electrochemical properties of the new fluorophosphate $LiNaFe[PO_4]F$. *Dalton Trans.* **41**, 11692–11699 (2012).
27. Dong, H. et al. Compression of lithium fluoride to 92 GPa. *High Press. Res.* **34**, 39–48 (2014).
28. Fukuhara, M. Lattice expansion of nanoscale compound particles. *Phys. Lett. A* **313**, 427–430 (2003).
29. Ahmad, M. I. & Bhattacharya, S. S. Size effect on the lattice parameters of nanocrystalline anatase. *Appl. Phys. Lett.* **95**, 191906 (2009).
30. Tsunekawa, S., Ishikawa, K., Li, Z. Q., Kawazoe, Y. & Kasuya, A. Origin of anomalous lattice expansion in oxide nanoparticles. *Phys. Rev. Lett.* **85**, 3440–3443 (2000).
31. Szczęśniak, M. M. & Ratajczak, H. Ab initio calculations on the lithium fluoride–ethylene complex. *J. Chem. Phys.* **67**, 5400–5401 (1977).
32. Hahn, H. & Strick, G. Zur Mischkristallbildung zwischen Lithiumfluorid und Lithiumhydrid. *Z. Anorg. Allg. Chem.* **372**, 248–251 (1970).
33. Varotsos, P. A. & Mourikis, S. Difference in conductivity between LiD and LiH crystals. *Phys. Rev. B* **10**, 5220–5224 (1974).

Methods

Electrochemical measurements. The electrolytes of interest were prepared by dissolving the conductive salt LiFSI (Nippon Shokubai) in three solvents at different concentrations (1 M and 5 M) inside an MBRAUN glovebox filled with purified argon, where the moisture and oxygen levels were <1 ppm. In selecting the solvents to be used, we chose PC, DMC and DME over ethylene carbonate which is a good component for lithium-ion batteries but not for lithium metal batteries. As suggested by previous work[34], lithium metal batteries will fade quickly (<20 cycles) in realistic 300 Wh kg^{-1} lithium metal pouch cells if ethylene carbonate is used as the cosolvent due to the high impedance of the SEI derived from ethylene carbonate. In the choice of concentration, both a low concentration (1 M) and a high concentration (5 M) are used as they are expected to have very different solvation structures, and hence different SEI chemistries. Battery-grade PC, DMC and DME solvents were obtained from BASF Battery Materials. To monitor the CE of six different electrolytes, coin-type Li||Cu cells (CR2032) were assembled using the same glovebox as above. All coin cells were configured with a copper disc (25.6 μm thickness), a lithium disc (15.7 mm diameter, 450 μm thickness; MTI Corp.) and a piece of polyethylene separator (Hipore, Asahi Kasei). Each cell includes 75 μl of electrolyte. Galvanostatic lithium plating/stripping of Li||Cu cells was performed using a curtailed capacity of 1 mAh cm^{-2} and then a 1.0 V cutoff upon the stripping process at a constant current (0.5 mA cm^{-2}). All cells were cycled 50 times in order to obtain the proper amount of SEI for the SEI characterizations.

Sample preparation. Cell disassembly and SEI preparation processes were performed in an argon-filled glovebox. The SEI films and powders accumulated on the electrodes were soaked together in the DMC solvent (Gordon). As an invasive method, the SEI was separated from the copper and native lithium electrodes by physical shaking of the DMC-containing vial, and then the electrodes were removed from the SEI-dispersed solution. After that, the solid SEI was separated through vacuum filtration using customized apparatus. This process was repeated with pure DMC solvent to remove the residual solvent within the SEI matrix. The filtered solid SEI was dried overnight in the small antechamber of the glovebox under vacuum at room temperature. As the SEI sample collection method in this work is invasive, spatial information is inevitably lost; however, the chemical information of the SEI is well preserved. The masses of SEI samples collected in HCE and LCE were about 2 and 5 mg, respectively. Each SEI came from three coin cells that showed exactly the same electrochemical profile during cycling. Each SEI sample was carefully transferred and densely packed into a polyimide capillary (Cole-Parmer), which was then hermetically sealed using epoxy glue. In an effort to preserve the original state and to avoid contamination, the samples were rinsed thoroughly before drying to ensure any electrolyte residue was removed. It is worth noting that since our samples were collected after cell disassembly, only non-dissolvable components were preserved. The dissolvable components should have already been dissolved in the electrolyte during cycling and will have had little effect on the functionality of the SEI. The SEI samples in this work were collected on a copper counter electrode. The effects of the counter electrode (copper or lithium) on the formation of the SEI may need further investigation. The differences in the shear viscosity and density of the electrolytes containing LiFSI in different carbonate solvents at different concentrations are quite important[35] and their effects on the SEI phase stability may also need further investigation.

XRD and PDF data. XRD and PDF data were collected at beamline 28-ID-2 of the National Synchrotron Light Source II using a photon wavelength of 0.18323 Å. In some experiments, a wavelength of 0.1917 Å was used. Samples were spun during the measurement at a spin speed of 2 revolutions per second to avoid inaccuracy in XRD quantification caused by texture. XRD and PDF data were collected using an amorphous silicon flat panel two-dimensional detector (Perkin Elmer) and radially integrated using Fit2D software[36]. The beam size used in this work was 1 × 1 mm. The exposure time of ex situ measurements was typically around 0.5 h for XRD and 1 h for PDF. The PDF and $G(r)$ values were extracted using PDFgetX3 software[37].

In situ air-exposure measurements. The sample with a relatively high LiH content was selected for the air-exposure experiment. After the epoxy glue had been removed from the capillary, the XRD patterns were immediately collected every 90 s.

DFT calculations. All DFT calculations were performed using the Vienna ab initio simulation package (VASP) with a projector augmented-wave (PAW) approach[38,39]. For the structure relaxation of molecule LPDC, LMC and the LMC dimer, we adopted a generalized gradient approximation-type exchange-correlation functional in the parameterization by Perdew, Burke, and Ernzerhof[40]. The relaxation was done in a cubic cell of 30 × 30 × 30 Å. A k mesh of a single k point at the Γ centre of the first Brillouin zone was used. For all calculations the wave-function and charge-density cutoffs were 500 and 756 eV, respectively. For the relaxations of the molecule structures, the forces felt by each of the atoms were well converged below 0.001 eV $Å^{-1}$.

Data availability

All relevant data in the article are available from the corresponding author upon reasonable request.

References

34. Niu, C. et al. High-energy lithium metal pouch cells with limited anode swelling and long stable cycles. *Nat. Energy* **4**, 551–559 (2019).
35. Neuhaus, J., von Harbou, E. & Hasse, H. Physico-chemical properties of solutions of lithium bis(fluorosulfonyl)imide (LiFSI) in dimethyl carbonate, ethylene carbonate, and propylene carbonate. *J. Power Sources* **394**, 148–159 (2018).
36. Hammersley, A. P., Svensson, S. O., Hanfland, M., Fitch, A. N. & Hausermann, D. Two-dimensional detector software: from real detector to idealised image or two-theta scan. *High Press. Res.* **14**, 235–248 (2006).
37. Qiu, X., Thompson, J. W. & Billinge, S. J. L. PDFgetX2: a GUI-driven program to obtain the pair distribution function from X-ray powder diffraction data. *J. Appl. Crystallogr.* **37**, 678 (2004).
38. Blöchl, P. E. Projector augmented-wave method. *Phys. Rev. B* **50**, 17953–17979 (1994).
39. Kresse, G. & Furthmüller, J. Efficiency of ab-initio total energy calculations for metals and semiconductors using a plane-wave basis set. *Comput. Mater. Sci.* **6**, 15–50 (1996).
40. Perdew, J. P., Burke, K. & Ernzerhof, M. Generalized gradient approximation made simple. *Phys. Rev. Lett.* **77**, 3865–3868 (1996).

Acknowledgements

The work done at Brookhaven National Laboratory was supported by the Assistant Secretary for Energy Efficiency and Renewable Energy, Vehicle Technology Office of the US Department of Energy (DOE) through the Advanced Battery Materials Research (BMR) Program, including Battery500 Consortium under contract no. DE-SC0012704. The work done at Pacific Northwest National Laboratory was supported by the Assistant Secretary for Energy Efficiency and Renewable Energy, Office of Vehicle Technologies of the US DOE through the Advanced Battery Materials Research (BMR) Program (Battery500 Consortium) under contract no. DE-AC02-05CH11231. The work at the Army Research Laboratory was performed under JCESR, an Energy Research Hub funded by Basic Energy Sciences, US DOE. This research used beamline 28-ID-2 of the National Synchrotron Light Source II, a US DOE Office of Science user facility operated for the DOE Office of Science by Brookhaven National Laboratory under contract no. DE-SC0012704.

Author contributions

J.X., E.H. and X.-Q.Y. proposed the research. J.X., J.L. and X.-Q.Y. organized and guided scientific discussions. H.L. and X.C. performed electrochemical characterization and SEI sample preparation. Z.S., X.W., O.B., S.G., C.W., X.F., S.-M.B., R.L. and E. H. performed XRD and PDF measurements and carried out the analysis. Z.S., J.X., E.H., K.X. and X.-Q.Y. prepared the manuscript with critical input from all other authors.

Competing interests

The authors declare no competing interests.

Additional information

Supplementary information is available for this paper at https://doi.org/10.1038/s41565-020-00845-5.

Correspondence and requests for materials should be addressed to J.X., X.-Q.Y. or E.H.

Peer review information *Nature Nanotechnology* thanks Marcella Bini, Donal Finegan and the other, anonymous, reviewer(s) for their contribution to the peer review of this work.

Reprints and permissions information is available at www.nature.com/reprints.